Mechanically Compatible UV Photodetectors Based on Electrospun Free-Standing Y³⁺-Doped TiO₂ Nanofibrous Membranes with Enhanced Flexibility

Ziliang Li, Mahesh K. Joshi, Jiaxin Chen, Zhiming Zhang, Ziqing Li, and Xiaosheng Fang*

Free-standing flexible TiO₂ nanofibrous membranes (NFMs) are highly desired for the construction of high-performance wearable electronic devices. Nevertheless, tremendous challenges still exist due to the fragile characteristics of the polycrystalline TiO₂ nanofibers. Here, ultra-flexible TiO₂ NFMs with robust fatigue strength and photoelectric properties are achieved via a simple element doping approach and the electrospinning technique. The 2 mol% Y³⁺-doped NFM-based photodetector exhibits excellent UV detecting performance at 3 V under 350 nm illumination, that is, responsivity of 4.5 A W⁻¹, detectivity of 1.6×10^{11} Jones, and photocurrent of ≈1.6 μA. By effectively tuning the distribution and bonding state of Y³⁺ ions, the NFM shows significantly enhanced flexibility, where its original photocurrent is successfully maintained in various bending states (angle, radius, spiral state). Importantly, the resultant Y³⁺-doped TiO₂ NFM maintains ≈60% of its original photocurrent after bending at ≈145° for more than 20 000 times. A plausible prototype accounts for the effective bending deformation mechanism is proposed on the basis of the systematic analyses of the microstructural characteristics and the stress distribution achieved by using the finite element method. Finally, a wearable UV monitoring system that outputs real-time photocurrent signals with different motion combinations of the remote-controlled robot is demonstrated.

1. Introduction

Ultraviolet (UV) radiation has huge impact on the survival and evolution of the earth's biological, even it only accounts for less than 10% of the total solar radiation.[1] Thanks to the existence of the ozone layer at the outermost layer of the earth's atmosphere, the majority of UV-C (100–280 nm) radiation can be blocked off, however, UV-B (280–320 nm) and UV-A (320–400 nm) radiation can penetrate and ultimately become the chief culprit for many serious diseases, for example, skin pigmentation, DNA damage, erythema, apoptotic cell death, skin cancer, etc.[2] For better forewarning the UV radiation, semiconductor-based UV photodetectors (PDs), which can convert UV radiation signals to electronic signals according to the photoelectric effect, have been extensively investigated and applied in many areas, such as environmental monitoring, space communications, flame detection, and so on.[2a,2d,3] In the past decade, real-time wearable UV monitoring devices have attracted increasing attention because of their distinct advantages, such as intelligence, flexibility, and functionality, which are highly desired for the prevention of skin diseases caused by excess UV exposure.[2d,4] Therefore, selecting appropriate materials with high photoelectric performance and mechanical flexibility is highly desired for the construction of wearable UV irradiation monitoring systems.[4a,5]

As one of the most widely investigated inorganic semiconductors, titanium dioxide (TiO₂) is an important n-type semiconductor material with many advantages, e.g. high chemical stability, nontoxity, wide direct band gap (≈3.2 eV, anatase; ≈3.0 eV, rutile) and superior electron transport properties, enabling it to be one of the most competitive sensitive material candidate for the construction of UV PDs in selective UV wavelength ranges.[3a,6] However, the pristine TiO₂ nanofibers suffer from their fragile nature and can easily break into fine powders,[7] causing a series of issues such as serious degradation of responsivity and detectability as a wearable UV PD device which hinders their further applications. In this regards, extensive research efforts have been conducted on the fabrication of TiO₂ materials with reduced dimension (D), such as 0D, 1D, 2D, and 3D nanostructures via a series of techniques, such as sol–gel, hydrothermal, solvothermal, wet-chemical, thermolysis, and electrodeposition.[8] Among them, 1D TiO₂ nanostructures with enhanced mechanical flexibility, for example, nanotubes,[2d,9] nanorods,[10] nanofibers,[11] and nanowires[12] have stimulated much attention in high performance UV PDs owing to pronounced surface effects (i.e., oxygen adsorption/desorption) originating from the large surface-to-volume ratio.[6a,13] Nevertheless, previous works are mainly on the basis of the integration of nanostructure materials on soft substrates

Dr. Z. Li, J. Chen, Dr. Z. Zhang, Dr. Z. Li, Prof. X. S. Fang
Department of Materials Science
Fudan University
Shanghai 200433, P. R. China
E-mail: xshfang@fudan.edu.cn
Prof. M. K. Joshi
Department of Chemistry
Tribhuvan University
Tri-Chandra Multiple Campus, Kathmandu 44613, Nepal

The ORCID identification number(s) for the author(s) of this article can be found under https://doi.org/10.1002/adfm.202005291.

**ADVANCED
SCIENCE NEWS**
www.advancedsciencenews.com

**ADVANCED
FUNCTIONAL
MATERIALS**
www.afm-journal.de

(e.g., plastic or polymers), which bring forward strict requests for the materials compatibility, processing techniques and also inevitably introduce undesirable volume of the device.[14,15] In this case, it is highly desirable to develop a facile and effective method for the preparation of free-standing TiO_2 nanostructures with high photoelectric properties and robust flexibility.[2d,5a]

Electrospinning is a very versatile and straightforward technique to produce 1D nanofibers of high quality with controllable dimensions and nanostructures.[16] Through simple modifications, various free-standing inorganic nanofibrous membranes (NFMs) with excellent mechanical properties have been achieved via electrospinning and appropriate post treatment for many applications such as catalysis, sensors, solar cells, tissue engineering, PDs, and so on.[16a,17] Specially, the electrospun TiO_2 NFM displays high photoelectric performance,[18] and their mesh structure makes it possible for the stress relaxation during bending and also gives this structure more effective UV illumination area for the construction of high-performance PDs.[19] Nevertheless, the polycrystalline nature of the TiO_2 nanofibers usually induces mechanically fragile, which hinders their further application in many areas.[12,20] So far, only a few mechanically improved electrospun TiO_2-based NFMs have been investigated, such as Y^{3+}-doped TiO_2 NFMs with a tensile strength of 472.5 kPa[21] and the substitutional doping of Zr^{4+} could effectively enhance the tensile strength and bending resistance of more than 200 times.[7] However, the TiO_2 NFMs-based PDs with high tensile strength and bending resistance which are suitable for constructing functional wearable electronic systems are still lack of investigation. Therefore, it is still an imperative challenge to develop flexible TiO_2 NFMs-based UV PDs with simultaneously enhanced mechanical properties and photoelectric performances.

With those backgrounds and objectives in mind, in this work, we will present a wearable UV PD design with excellent photoelectric and mechanical properties based on Y^{3+}-doped TiO_2 NFMs. The photoelectric performance remains stable with Y^{3+} concentration up to 2 mol%, even when the PDs are exposed in different deformation states, such as bending angle, bending with different radius, in different spiral states, etc. More importantly, it can bear continuous bending (≈145°) for more than 20 000 times and the photocurrent remains ≈60% of its initial level. We propose a plausible explanation that artfully transforms fragile inorganic materials into flexible ones by simply elements doping and their distribution control, on the basis of a series of microstructural characterization techniques and the finite element method. Finally, the flexible UV sensitive material is successfully applied through the install of the PDs in a robot arm and a real-time wearable application is achieved. This work not only displays a promising method that can transform inorganic materials into free-standing soft ones which can meet the requirements in wearable UV detecting devices, but also provides a general and effective strategy for developing real-time and wearable electronic devices with high mechanical and functional performances.

2. Results and Discussion

2.1. Morphological Characterization

Figure 1a,b display typical optical photographs of the pristine and Y^{3+}-doped TiO_2 NFMs, respectively, which are prepared following the electrospinning and the calcination process
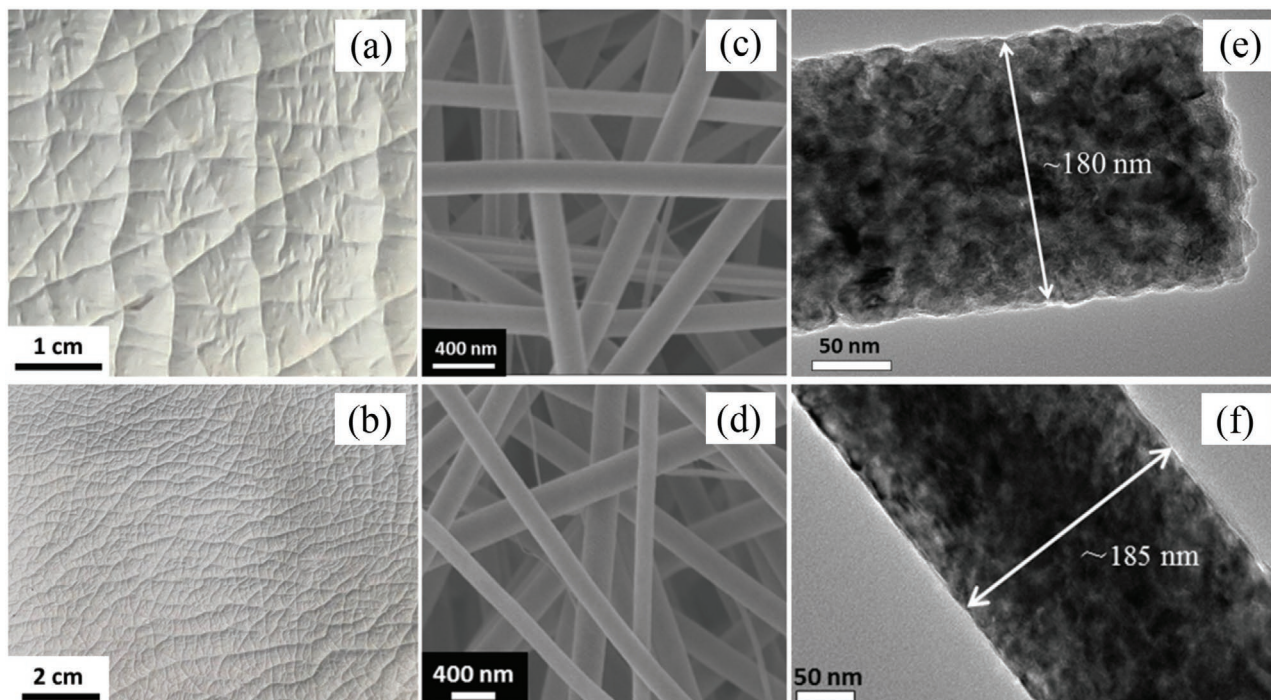

Figure 1. Photographs of the a) pristine and b) Y^{3+}-doped TiO_2 NFMs after calcination. FE-SEM images of the c) pristine and d) Y^{3+}-doped TiO_2 NFMs. Low-magnification TEM images of a single e) pristine and f) Y^{3+}-doped TiO_2 nanofiber.

(illustrated in the experimental section). It is clearly observed that we can obtain large-scale continuous TiO_2 NFMs with high density of skin-like wrinkles, which is mainly due to the shrinkage of membranes related to the evaporation of polymer composition (i.e., PVP) and stress relaxation during the calcination process.[16a,22] A further check of the microstructure of the TiO_2 NFMs is conducted by high-resolution field emission scanning electron microscope (FESEM), the results indicate that the fibers in both membranes are homogeneously cross-aligned in a 3D mesh format, as shown in Figure 1c,d. It is noteworthy that the electrospun fibers present dense and smooth surface with homogeneous diameter of ≈180 nm, as shown in the low-resolution transmission electron microscope (TEM) images of single nanofibers (Figure 1e,f). The results reveal that dense and uniform TiO_2 nanofibers without obvious microscopic surface defects can be successfully acquired based on the selected processing route. No obvious microstructural difference can be observed when comparing the microstructure of the pristine and Y^{3+}-doped NFMs, implying that the doping of Y^{3+} in a certain content has no clear influence on the morphological characteristics of the TiO_2 NFMs when the same electrospinning and calcination process are applied. Generally, dense and homogeneous nano-sized fibers are favorable microstructure for achieving high mechanical properties, attributing to the reduced surface and internal micro-defects which are beneficial to the flexibility.[22,23] Importantly, the samples could be twisted and folded without any damage (see Figure S1, Supporting Information), indicating excellent flexibility of the electrospun TiO_2 NFMs. This achievement should be benefited from a combination of the reduced diameter, the distinct microstructure and the effective slippage between cross-aligned nanofibers in the NFMs.[7,24] The

excellent flexibility of the electrospun TiO_2 NFMs is a critical factor for their efficient application in the construction of soft or wearable UV PDs.

2.2. Evaluation of the Photoelectric Performances

The photoelectric properties of the pristine and the Y^{3+}-doped TiO_2 NFMs are characterized by constructing them into planar PDs using Au/Cr electrodes, the device structure is schematically depicted in **Figure 2**a. The Y^{3+} ions concentration can reach up to 2 mol% with comparable photoelectric performance with the pristine TiO_2 NFM; see Figure S2a, Supporting Information. Figure 2b presents the current–voltage (I–V) characteristics of the 2 mol% Y^{3+}-doped TiO_2 NFM-based planar PDs under dark and 350 nm (0.62 mW cm^{-2}) UV light illumination. The photocurrents under illumination are distinctively enhanced compared with the corresponding dark currents, giving large I_{photo}/I_{dark} ratio of ≈2.4 × 10^4, which is clearly enhanced compared with the pristine TiO_2 NFM (Figure S2b, Supporting Information). Such an improvement is mostly associated with the remarkable decreased dark current that originates from the blocking effect related to the generation of excess crystallographic defects induced by element doping.[5a] On the other hand, considerate defect engineering in PDs can enhance the light absorption and prolong the photocarrier lifetime, and thus gives an effective compensation of the photocurrent decay. In order to reveal the device stability and the response speed of the 2 mol% Y^{3+}-doped TiO_2 NFM, the current–time transient response (I–t) characteristics are measured under 3V bias and 350 nm, as shown in Figure 2c. It is noteworthy that the 2 mol% Y^{3+}-doped TiO_2 NFM displays high
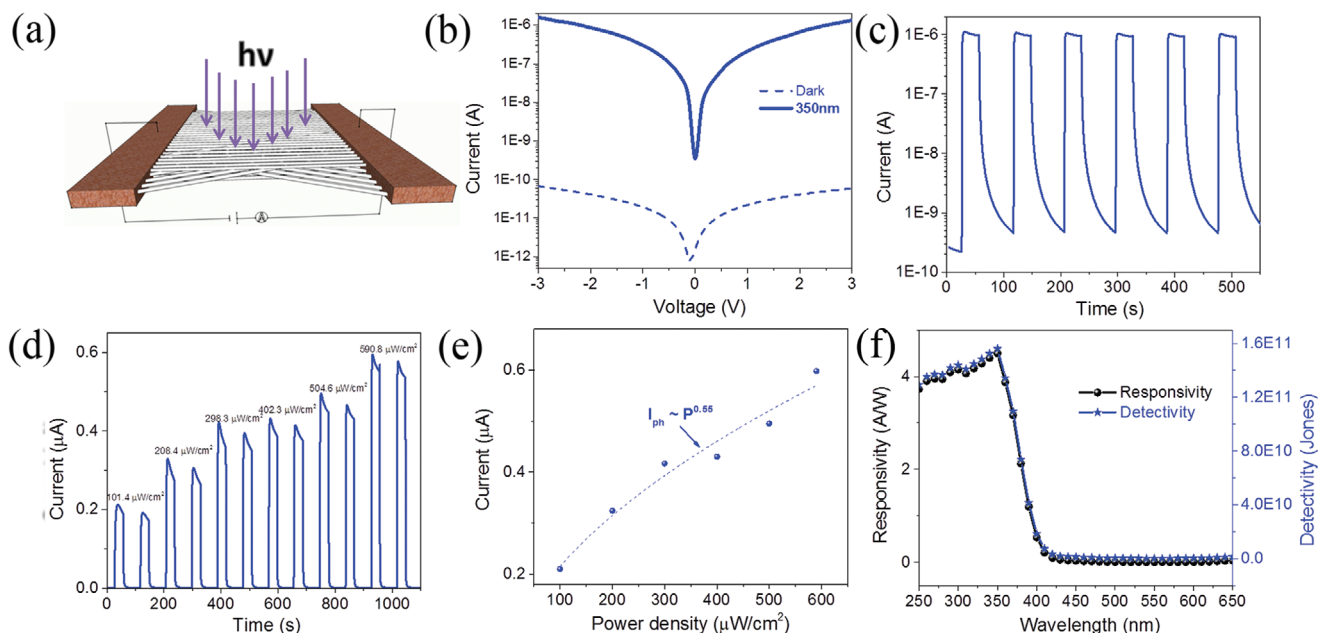

Figure 2. Photoelectric performances of the 2 mol% Y^{3+}-doped TiO_2 NFM-based planar PD: a) Schematic diagram of the plannar PD. b) I–V curves under dark and light luminance of 350 nm (0.62 mW cm^{-2}). c) I–t curves measured at 3 V bias and 350 nm (0.62 mW cm^{-2}) light illumination. d) I–t curves measured at 3 V bias and 350 nm light illumination with different power density. e) Photocurrent evolution as a function of power density. f) Calculated responsivity and detectivity curves of the planar PD.

ADVANCED
SCIENCE NEWS
www.advancedsciencenews.com

ADVANCED
FUNCTIONAL
MATERIALS
www.afm-journal.de

photoelectric performance, reaching stable photocurrents of ≈1 µA immediately after exposure to incident light and remains a high on/off ratio of ≈10^3 under a 3 V bias. After several on/off repetitions, the photocurrent remains stable and exhibits excellent repeatability. Moreover, photocurrents of the pristine and 2 mol% Y^{3+}-doped TiO_2 NFM-based PDs display rise times of 3.47 and 2.53 s as well as decay times of 3.83 and 1.16 s (see Figure S2c, Supporting Information), respectively, demonstrating that the incorporation of Y^{3+} within TiO_2 polycrystalline fibers has promoted the rapid response of the light illumination. The accelerated photoresponse is probably attributed to the emergence of defects (e.g., oxygen vacancies, grain boundaries, etc.) induced trap states, which can promote the photogenerated charge carriers recombination and ultimately lead to the rapid response of the light illumination.[2c]

The influence of light power density on the current response behaviors of the TiO_2 NFMs-based PDs have also been investigated under 3 V bias and 350 nm UV light illumination, the results are shown in Figure 2d. Obviously, the 2 mol% Y^{3+}-doped NFM-based PD displays stable response with similar response speed to light with different power densities, which is similar as the pristine TiO_2 NFM-based PD (Figure S2d, Supporting Information), consistent with the fact that the concentration of photogenerated carriers is positively correlated to the absorbed photon flux.[25] In this scenario, the photocurrents (I_{ph}), is usually described as a function of photodensity according to the power law:[26]

$$I_{ph} = \alpha P^{\theta} \tag{1}$$

where α is a constant under certain wavelength, and the exponent θ determines the response of the photocurrent to light intensity. The exponent θ of the 2 mol% Y^{3+}-doped NFM-based PD is fitted to be 0.55 (Figure 2e), which is different from the pristine TiO_2 NFM (0.91, Figure S2e, Supporting Information). The fractional power dependence is suggested to be related to the complex processes of electron–hole generation, recombination, and trapping effects for the device.[11,27] To reveal the spectral response of the TiO_2 NFMs-based PDs, the responsivity is calculated according to the following equation,[28]

$$R_{\lambda} = \frac{I_{ph} - I_d}{P_{\lambda} S} \tag{2}$$

where I_d is the dark current, P_{λ} is power density of the incident illumination, S is the effective area under irradiation, and λ is the excitation wavelength. Figure 2f presents the spectral response of the Y^{3+}-doped TiO_2 NFM-based PD at 3 V bias from 250 to 650 nm. Obviously, the PD shows notable photoresponses from 250 to 400 nm while a sharp cut-off edge can be clearly seen at the wavelength of 380 nm, showing a highly selective detection to UV light from stray visible light source. Another important merit to evaluate a PD is the detectivity (D^*, typically quoted in Jones), which reflects the ability to detect weak signals from the noise environment. Assuming the shot noise from the dark current is the major contributor of background noise, the D^* can be estimated by the following formula,[29]

$$D^* = \frac{R_{\lambda}}{\left(2e\, I_d/S\right)^{1/2}} \tag{3}$$

where e stands for the elementary charge (1.6×10^{-19} A s). The D^* of the Y^{3+}-doped TiO_2 NFM achieves as high as 1.6×10^{11} Jones at the wavelength of 350 nm (Figure 2f, blue curve) and it keeps the highest value in the wavelength range of 250–360 nm, which completely exceeds the pristine TiO_2 NFMs (Figure S2f, Supporting Information) owing to the suppressed dark current. Overall, the planar TiO_2 NFM-based PDs display excellent photoelectric properties, implying that they are promising material candidates for the construction of high performance photoconductive detector.

Another important requirement that a flexible UV PD should meet is its excellent photoelectric performance when operates upon single and/or repeated in various mechanical deformation states (bending, folding, etc.) without considerable decrease of their photoresponse performances.[30] In this case, it is also necessary to evaluate the photoelectric stability of the electrospun TiO_2 NFMs under different bending states and repeated mechanical deformations, with the presence of the optical images for illustrating the bending states in Figure S3, Supporting Information. The photoresponse behaviors of the TiO_2 NFMs-based PDs are measured with different bending radii (i.e., $R = 3.76, 7.12, 11.74, 24.75,$ and 33.80 mm) under dark and 350 nm (0.62 mW cm^{-2}) illumination, as shown in **Figure 3**a. In contrast to the dramatically declined currents with the decrease of bending radius for the pristine TiO_2 NFM, the currents of the 2 mol% Y^{3+}-doped TiO_2 NFM keep very stable when reducing the bending radius even down to 3.76 mm, revealing that the doping of Y^{3+} with a proper concentration ensures an efficient enhancement of the flexibility and thus the stable photoelectric performance during the external bending process. The result is fairly in agreement with the previous reports on the photoresponse behaviors of TiO_2 NFM, where the bending induced decline of photocurrent is mainly due to the crack of the nanofibers during the bending process taking into account that the inexistence of piezoelectric effect of TiO_2.[10,12] The mechanical flexibility and photoelectrical stability of the electrospun TiO_2 NFMs has also been evaluated by controlling the PD to specific bending angles, ranging from 0° to 180° with a shape tip (Figure S3c, Supporting Information). Figure 3b displays the normalized photocurrents as a function of the bending angles. Under bending states, the Y^{3+}-doped TiO_2 NFM-based PD demonstrates no discernible degradation of photocurrents at bending angles between 0° and 145°, and only ≈20% degradation occurs when the bending test is conducted at 180°. The result illustrates that the Y^{3+}-doped TiO_2 present superior photoelectric stability in different bending angles when compared to either the pristine TiO_2 NFM or other 1D nanostructures.[30b] The construction of free-standing NFMs into a 3D helical structure is of particular interest in the field of wearable electronic devices, because of the significantly enhanced mechanical strain it can bear.[31] In this instance, the photoelectric performance of the Y^{3+}-doped TiO_2 NFM-based PD has also been tested in a spiral bending condition (see Figure S3d, Supporting Information), as shown in Figure 3c. As per the I–t curves of the PDs under spiral state, there is no obvious change in the photoelectric behaviors occurs after spiral bending, giving identical confirmation of the high potential that the electrospun NFM holds for further applications which require high strain and
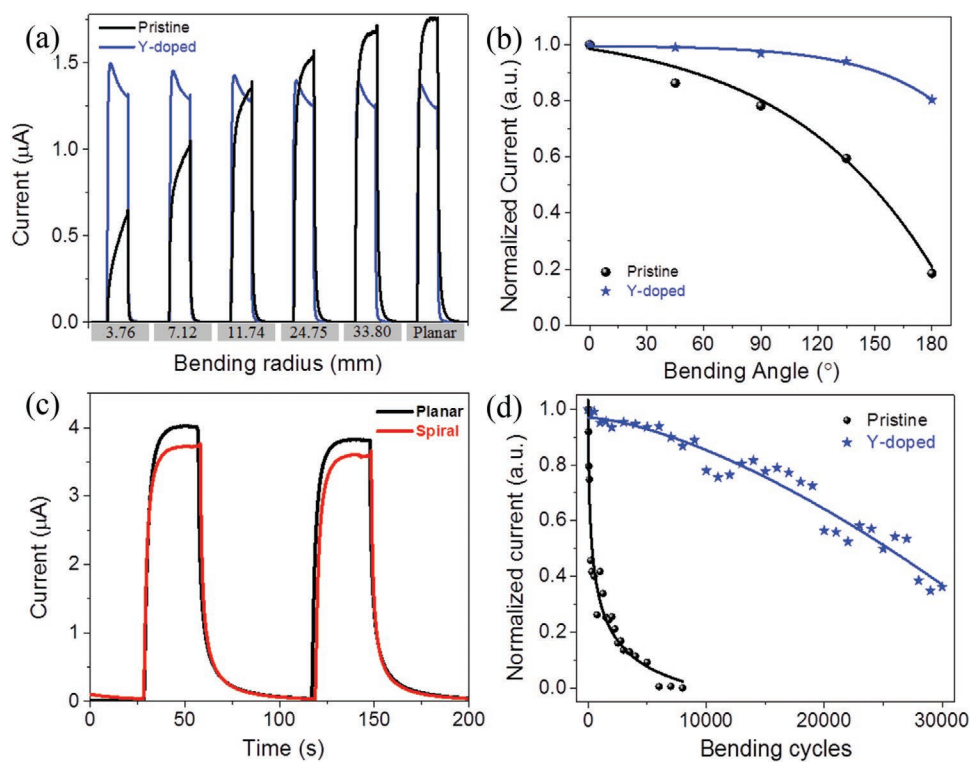
ADVANCED
SCIENCE NEWS
www.advancedsciencenews.com

ADVANCED
FUNCTIONAL
MATERIALS
www.afm-journal.de

Figure 3. Bending tests of the pristine and Y^{3+}-doped TiO_2 NFM-based PDs in different bending states: a) bending in different radius; b) bending in different angle; c) bending in a spiral state; d) bending in 145° for different cycles. All the measurements are conducted at 3 V and 350 nm (0.62 mW cm^{-2}) light illumination.

photoelectric performance.[31a,32] For the construction of a wearable photo-detecting device, the photoelectrical stability during continuous mechanical bending process, which inevitably introduces residual strain and sometimes even mechanical degradation or crack in TiO_2 NFMs during bending process, is also an essential factor should be taken into consideration. For conducting an effective cyclic bending test, the NFMs-based PDs are attached onto a PET as substrate and the photoelectric measurements are performed after bending for a certain bending angle of ≈145° and different times (see Figure S3e, Supporting Information). Figure 3d displays the normalized photocurrents evolution with bending cycles. It is observed that photocurrents of the pristine TiO_2 show significant degradation even during the initial bending state, decreased to ≈40% of the initial photocurrent after 50 bending cycles. Comparatively, the photocurrents of the Y^{3+}-doped TiO_2 could even keep ≈60% of the maximum value ultimately after bending for ≈20 000 times, which is superior compared with the previously reported 1D materials.[30] The degradation of the photocurrent is mainly attributed to the fracture of nanofibers (see Figure S4, Supporting Information).

Overall, both the photoelectric performances and mechanical properties of the Y^{3+}-doped TiO_2 NFM are obviously superior to that of the previously reported fiber-shaped PDs prepared via the electrospinning technique, as summarized in **Table 1**. In this stage, it is therefore reasonable to conclude that the excellent mechanical property stability, efficient photoresponse together with the free-standing nature of the electrospun Y^{3+}-doped TiO_2 NFM, enable it to be one of the most appealing

material candidates for applications in wearable optoelectronic technologies.

2.3. Microstructure and Flexibility

Figure 4a shows the X-ray diffraction (XRD) analysis of the TiO_2 NFMs with different molar percentages of Y^{3+}, from 0 to 4 mol%. It is observed that all the diffraction peaks could be assigned to the anatase phase of TiO_2 (JCPDS No. 21–1272), revealing the complete transformation from the precursor to the anatase TiO_2. No additional peaks corresponding to Y compound could be identified which is probably attributed, either to the small doping concentration of Y species that below the detection limit of XRD[33] or to the special distribution states of the Y^{3+} within TiO_2 matrix.[21] Note that there is no clear shift of the (101) anatase peak for the NFMs when doping with Y^{3+} ion (inset in Figure 4a), suggesting that the incorporation of Y^{3+} ions inside the TiO_2 nanofiber does not induce lattice distortion. The average grain size of the anatase TiO_2 crystallites is estimated from the integral breadth of XRD reflections by Debye–Scherrer formula using (101), (105), and (104) Bragg peaks of TiO_2. Figure 4b displays the (101), (105), and (104)-oriented TiO_2 grain size evolution with Y^{3+} doping amount of 0, 1, 2, and 3 mol%. For the pristine TiO_2 NFMs, the mean sizes of the (101), (105), and (104)-oriented grains are estimated to be ≈23.3, ≈18.2, and ≈10.2 nm, respectively. It is worth noting that the average TiO_2 grain size monotonically decreases with the increase of the Y^{3+}-doping amount until reach a plateau

Table 1. Comparison of photoelectric performances and flexibility of typical fiber-based PDs prepared based on the electrospinning technique.

PD	Substrate	Type	Photoelectric performance						Mechanical bending					Ref.
			Bias [V]	λ [nm]	I_{on}/I_{off}	I_{ph} [A]	R_{λ} [A W^{-1}]	[a)]A_{max} [°]	[b)]MC [%]	R_{mini} [mm]	MC [%]	Times	MC [%]	
ZnO-SnO$_2$	Polyimide	Nanowire array	2	300	$\approx 10^3$	2×10^{-9}	–	–	–	–	–	1000	≈ 91	[45]
SnO$_2$	PET	Nanobelts	100	254	10^2	5×10^{-7}	–	–	–	1	45	1000	91	[38]
TiO$_2$/perovskite	Mica	Nanotube array	1	350	2.5×10^4	4×10^{-8}	3	180	≈ 100	–		200	≈ 93	[46]
Pristine TiO$_2$	Mica	Nanofiber array	10	254	$\approx 10^3$	3.6×10^{-8}	–	–	–	5	78	–	–	[12]
[d)]PQT-12	PDMS/PET	Nanofiber array	50	470	5.9×10^3	3×10^{-10}	0.93	–	–	0.75	83.2 ± 6.9	1000	82.3 ± 6.7	[47]
ZnO	Ni wire textile	Nanorod arrays	1	365	$\approx 10^2$	4×10^{-5}	0.25	120	≈ 100	–	–	1000	94	[4a]
ZnO/PbS	mica	Nanowire array	10V	350	≈ 500	5×10^{-10}	0.051	180	≈ 100	–	–	200	≈ 93	[48]
Pristine TiO$_2$	Free-standing	NFM	5V	350	$\approx 10^4$	7×10^{-8}	4×10^{-3}	–	–	–	–	1000	90	[11]
Y^{3+}-doped TiO$_2$	Free-standing	NFM	3 V	350	10^4	1.6×10^{-6}	4.5	145	≈ 100	3.76	≈ 100	1000	≈ 97	This work
												20 000	≈ 60	

[a)]A_{max} = the maximum bending angle during the bending test; [b)]MC = the percentage of the maintained photocurrent after mechanical bending; [c)]R_{mini} = the minimum bending radius during the bending test; [d)]PQT-12 = 3,3''''—didodecylquarterthiophene.
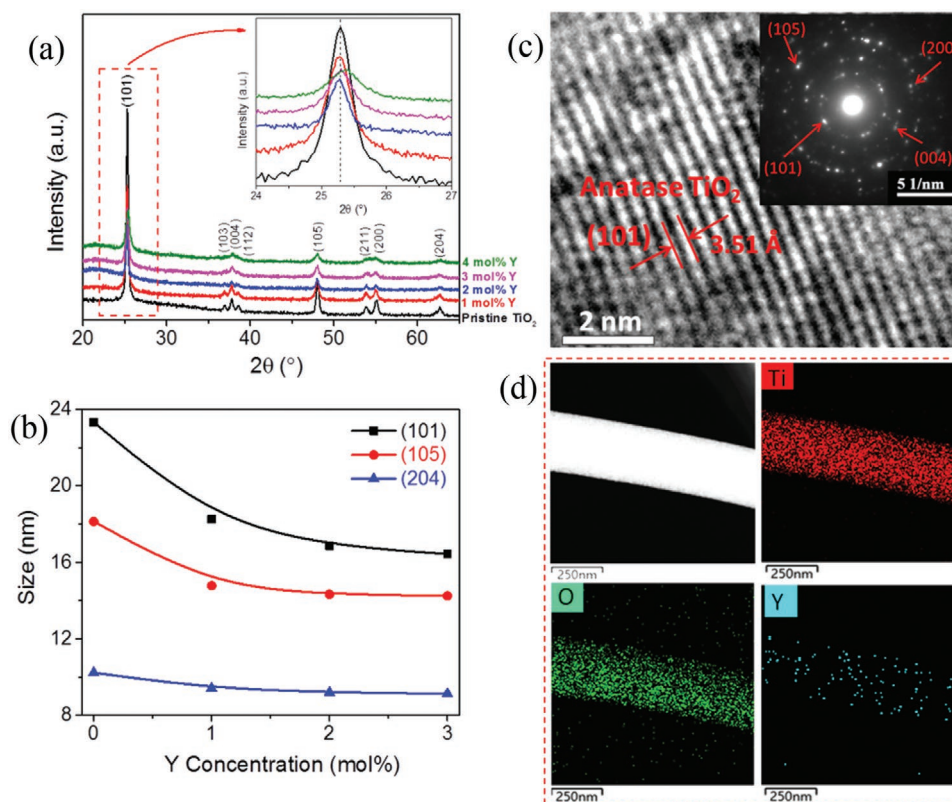

Figure 4. a) XRD patterns of the TiO$_2$ NFMs with different Y^{3+} doping amount of 0, 1, 2, 3, and 4 mol%, the inset displays the enlargement of the XRD peaks for the (101) plane. b) The evolution of the TiO$_2$ grain sizes for the TiO$_2$ NFMs with different Y^{3+} concentration. c) HRTEM image of the 2 mol% Y^{3+}-doped TiO$_2$ NFMs, the insert is a SAED pattern in selected area. d) EDS images of the 2 mol% Y^{3+}-doped TiO$_2$ NFM on a single fiber.

at the doping amount of 3 mol%. The grain coarsening of TiO_2 nanocrystalline phases is considerably controlled via Y^{3+}-doping, this is actually similar to the behaviors observed in the Zr^{4+},[7] Y^{3+},[21] and Y^{3+}-Ag^+[33] doped electrospun nanofibers. For a careful examination of the crystalline structure of flexible TiO_2 NFMs, we have performed high-resolution TEM (HRTEM) and EDS on the 2 mol% Y^{3+}-doped TiO_2 NFM, as shown in Figure 4c,d. The HRTEM image displayed in Figure 4c reveals that the interplanar distance of the lattice fringe derived from the (101) crystal plane of the anatase TiO_2 phase is calculated to be ≈0.35 nm, which is in consistent with the pristine anatase TiO_2.[21] The result demonstrates that Y^{3+} does not induce structural distortion of the anatase TiO_2 lattice, which is in good agreement with the previous XRD analysis. This conclusion is also confirmed by the detailed analysis of the UV–vis absorbance and electronic properties of the TiO_2 NFMs; see Figure S5, Supporting Information. The SAED pattern (Insert of Figure 4c) displays clear diffraction rings corresponding to the TiO_2 anatase phase, illustrating the polycrystalline structure of anatase phase with high crystal structure and without clear additional phase. From the EDS images presented in Figure 4d, it is clearly observed that the Ti and O elements are homogeneously dispersed throughout the nanofibers. However, the Y element is prone to distribute at the boundaries of TiO_2 grains in the form of tiny particles, in contrast with the previously reported element doped TiO_2 nanofibers.[7,21] Therefore, it is reasonable to conclude that the homogeneously distributed Y element at the grain boundaries may share the main

responsibility for reducing the atomic mobility and ultimately inhibits the coarsening of TiO_2 crystallites.

In order to reveal the surface composition and chemical states of the elements, we have conducted X-ray photoelectron spectroscopy (XPS) analyses of the Y^{3+}-doped TiO_2 NFMs and the results are displayed in **Figure 5**. Figure 5a shows the XPS survey spectra for the surface of the specimen, where the Ti, O, and Y elements are clearly identified. The Ti 2p displays doublet composed of 460.7 and 466.4 eV which corresponds to the Ti $2p_{3/2}$ and Ti $2p_{1/2}$, respectively, indicating that Ti appears as Ti^{4+}.[34] The two peaks of Ti 2p in the sample show the same energy levels as compared to the pristine TiO_2 NFM (Figure S6, Supporting Information), implying that the incorporation of Y^{3+} in the TiO_2 does not affect the chemical state of Ti element. The O 1s region can be fitted with two separated peaks located at 530.4 ± 0.2 and 532.0 ± 0.2 eV, respectively, as shown in Figure 5c. The first peak is assigned to the TiO_2 lattice oxygen and the second maybe related to the hydroxyl groups.[35] Noteworthy, the O 1s energy levels in the Y^{3+}-doped TiO_2 are slightly shifted toward lower energies compared with the pristine TiO_2 (see Figure S6c, Supporting Information), implying that the Y—O bond which located at ≈529.5 eV may be formed within the TiO_2 matrix.[36] Moreover, the Y 3d states are depicted in Figure 5d, in which the peak can be fitted in two separate energy level of 159.8 and 156.8 eV, respectively, implying that the Y element is in the oxide state, in agreement with the Y—OH bond reported in the previous literature.[37]
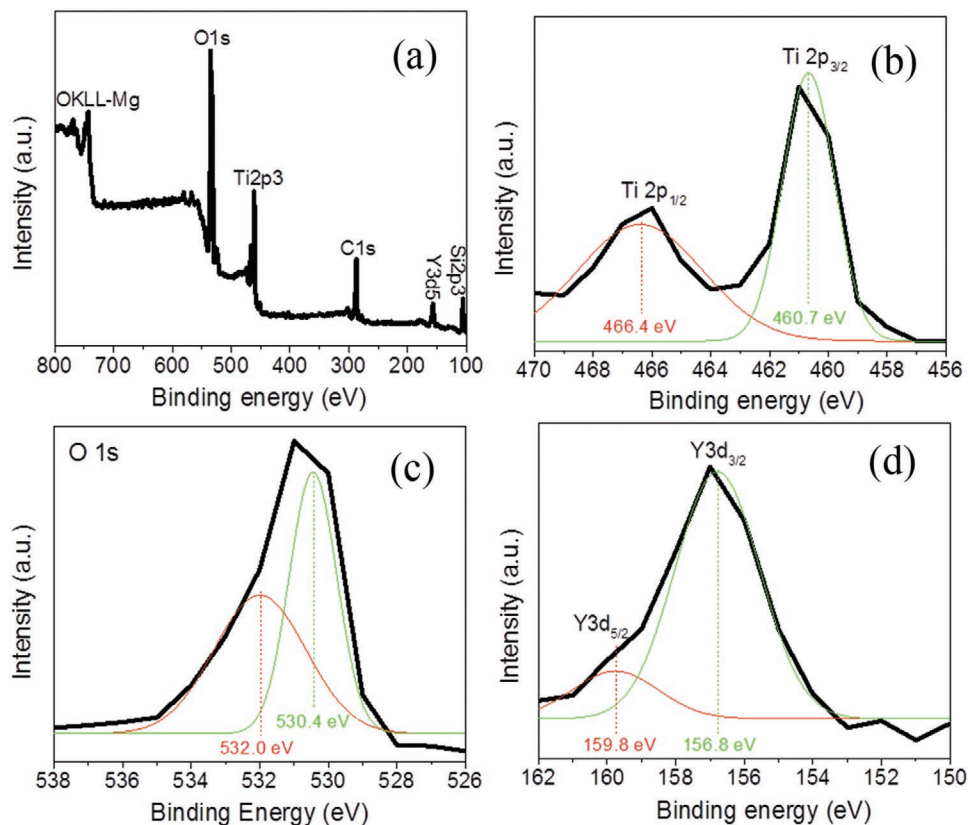

Figure 5. XPS spectra of the 2 mol% Y^{3+}-doped TiO_2 NFMs: a) survey scan, b) Ti 2p, c) O 1s, and d) Y 3d.
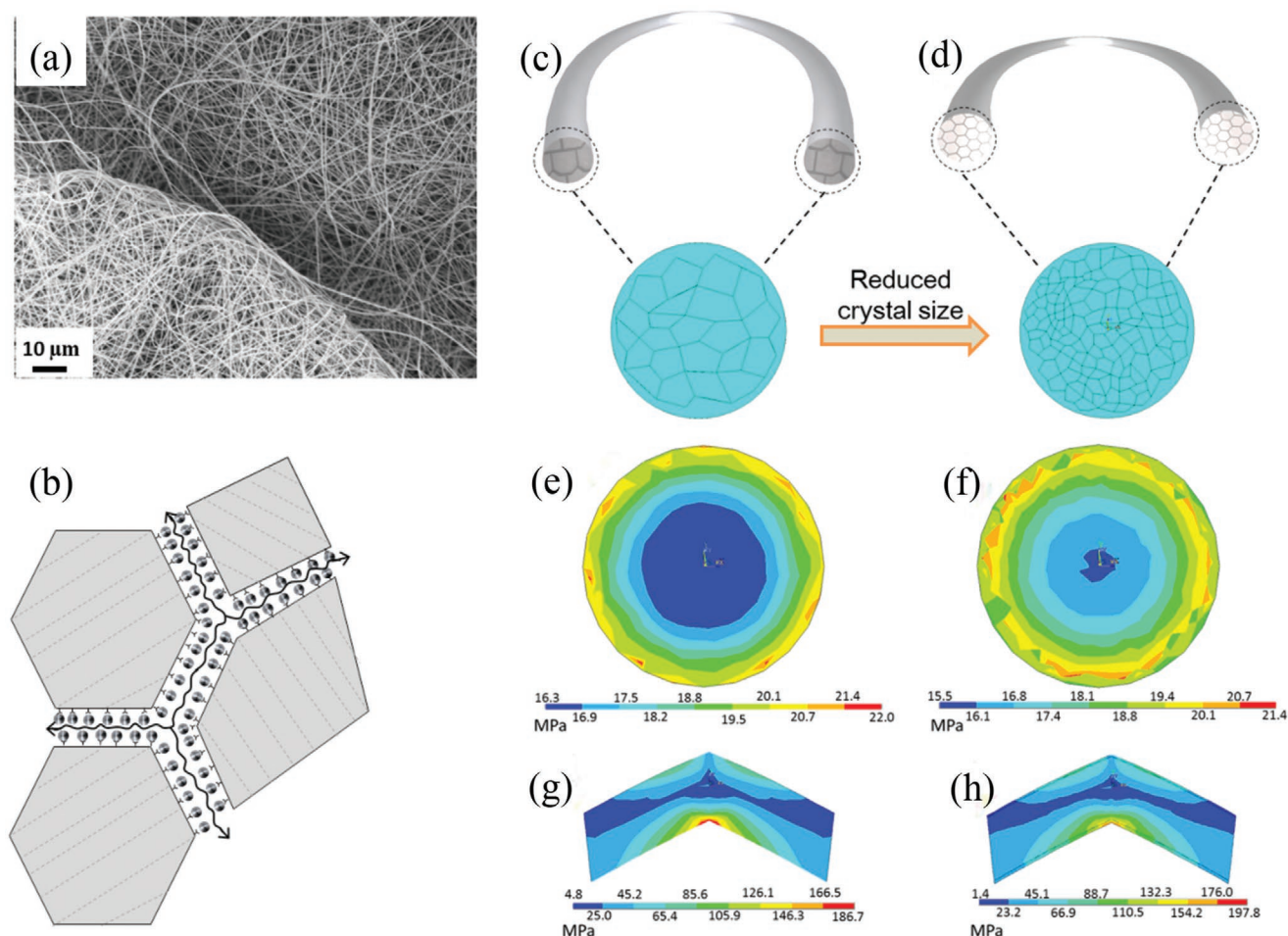
Figure 6. a) SEM image of the highly bended 2 mol% Y^{3+}-doped TiO$_2$ NFM. b) Schematic demonstration interpreting the plausible mechanism for the significant enhancement of the flexibility of the NFM based on the previous microstructural analyses. The cross-sectional demonstration of the nanofibers showing the simulation units of the c) pristine TiO$_2$ and d) Y^{3+}-doped TiO$_2$. The stress distribution at longitudinal section of the e) pristine TiO$_2$ and f) Y^{3+}-doped TiO$_2$. The stress distribution at transverse section of the g) pristine TiO$_2$ and h) Y^{3+}-doped TiO$_2$.

The excellent mechanical properties of the Y^{3+}-doped TiO$_2$ NFM can be further confirmed via a direct observation of its microstructural deviation in bending deformation. The continuous network and structural integrity of the electrospun NFM can be effectively maintained after severe bending deformation (**Figure 6**a), which benefits their superior structural flexibility by releasing the external stress through the interconnected relative sliding of nanofibers.[38] Additionally, it is also observed that the single nanofiber could tolerate extreme deformation with bending radius ≈600 nm (Figure S7, Supporting Information), which plays a critical role for enhancing mechanical flexibility of the NFM. In another word, an effective enhancement of the flexibility of the individual fibers plays a dominant role in further improving the softness of the TiO$_2$ NFMs.

The fracture of a nanofiber in bending states is generally correlated to the generation and extension of microcracks induced by stress concentration point associated to the crystal defects within ceramics.[24] In this scenario, we propose a plausible bending deformation mechanism for interpreting the remarkable mechanical flexibility of the Y^{3+}-doped TiO$_2$ NFMs over traditional ceramic materials, on the basis of the systematic

analysis of the microtructure of the TiO$_2$ fibers, as schematically illustrated in Figure 6b. The key point to the superior flexibility of the electrospun Y^{3+}-doped TiO$_2$ NFMs is related to the effectively reduced crystal size, which has been certified by the XRD method (Figure 4b). Long-range atomic diffusion is highly passivated due to the grain-boundary segregation, leading to the suppression of crystal growth.[39] The smaller crystal size and more dense-packed grains could efficiently scatter and dissipate the stress that suppresses the crack initiation and propagation in the fiber.[7,38,40] Furthermore, polycrystalline nanofibers with ultrafine grains could tolerate severe deformation owing to the enhanced strength and super plasticity caused by grain-boundary sliding following the Hall–Petch effect.[38,41] In contrast, for pure TiO$_2$ nanofiber, the excessive crystallite growth during calcination process may have either produced surficial defects or less slip system in the fiber which results a catastrophic failure when subjected to external force or load, the stress would condense on these defect areas as macro cracks propagate through the whole fiber.[7,39a] To better illustrate the effects of grain size on the generation, distribution and release of hydrostatic stress, the finite element method is

**ADVANCED
SCIENCE NEWS**

www.advancedsciencenews.com

**ADVANCED
FUNCTIONAL
MATERIALS**

www.afm-journal.de

used, as shown in Figure 6c–h. The simulation is conducted based on two different bending states, that is, a radius of 7 mm (Figure S8a, Supporting Information) and an angle of 45° (Figure S8b, Supporting Information), and irregular polygonal grain shapes (Figure 6c,d) have been taken with sizes referred to Figure 4b. It is worth reminding that the grains are set as paralleled fiber shapes along the nanofiber for the sake of simulation. Figure 6e–h compares the cross sectional stress profiles of both nanofibers in the two bending states, and the corresponding 3D stress distribution profiles are presented in Figure S8c–f, Supporting Information. It is clearly indicated in the stress nephograms that the pristine TiO_2 nanofiber (Figure 6e) shows a much sharper stress gradient compared to the Y^{3+}-doped TiO_2 nanofiber (Figure 6f) when bending in the radius of 7 mm. Moreover, large grain size is prone to induce stress concentration regions (see Figure 6g,h for the pristine and Y^{3+}-doped TiO_2 NFM, respectively), which promote the generation and extension of microcracks. It is therefore that mechanical failure is more likely to occur in larger grains, which is consistent with the reported experimental results.[42]

On the other hand, the tiny and homogeneous dispersed Y oxide (see Figure 4d), could act as reinforcement and solid lubricant for the relative slippage between grains, superadd the connection between grains by the Y—OH bonds as bridge which are preciously discussed in the XPS analysis, contributing to further dissipate external forces and yielding large deformation.[43] In addition, the grain-refinement and the fine distribution of Y oxide play crucial role in the enhancement of yield strength and elimination of surficial microcracks,

ultimately contributing to their resultant fatigue endurance life. Therefore, the Y^{3+}-doped TiO_2 fiber could exhibit high softness and cyclic behavior even under an extreme deformation.

2.4. Applications

To further demonstrate the versatility and validity of the free-standing flexible Y^{3+}-doped TiO_2 NFMs, a wearable UV monitoring system has been designed, as introduced in detail in Section 4 and the corresponding photograph is presented in **Figure 7**a. First, we have measured the static photoresponse of the UV detecting system in different index finger positions (where the full open, half open, and full close state of the finger has been marked as I1, I2, and I3, respectively) and the amount of UV lights (marked as L1, L2, L3, and L4). Figure 7b compares the $I–t$ curves of the UV monitoring system in a various positions with different amount of UV lights. Generally, the photocurrents under UV illumination are approximately three orders of magnitude larger than that in the dark state. The time dependent on/off photoresponse curves indicate that the system displays a rapid and stable sensitivity to UV light. Importantly, the photocurrents show clear fluctuation with the atmospheric change, demonstrating that the device is suitable for capturing slight deviation of atmospheric UV illumination change. This phenomenon is further reflected by the static $I–t$ measurements of the thumb (T), index finger (I), middle finger (M), ring finger (R), and little finger (L) in different states of full-open (1), half-open (2), and full-close (3), respectively, as
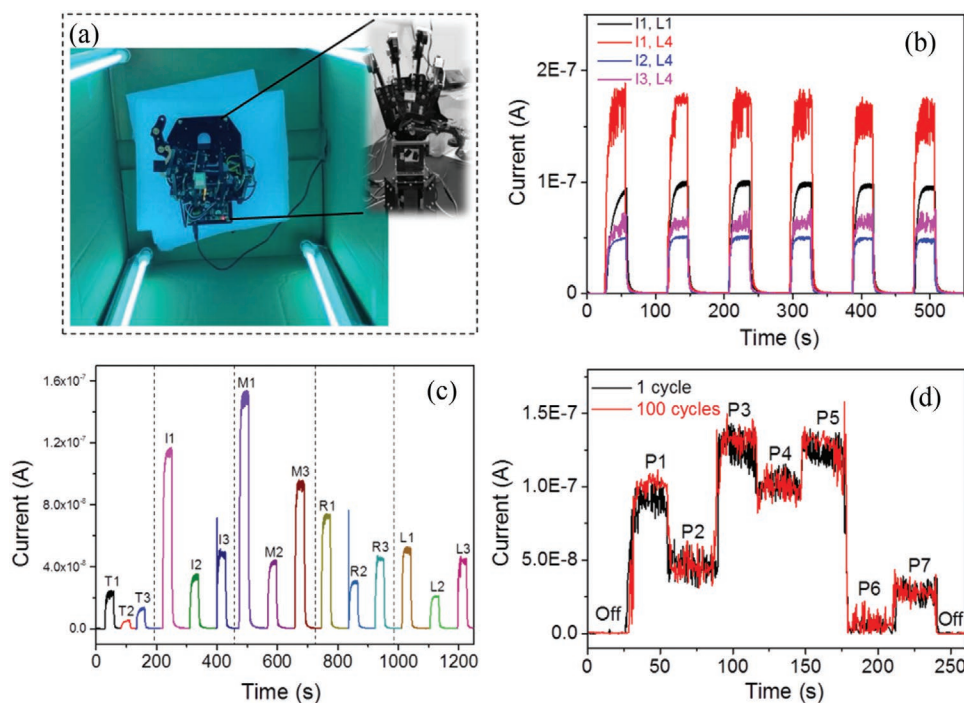

Figure 7. Demonstration of the flexible Y^{3+}-doped TiO_2 NFM-based wearable UV monitoring system. a) Photographs of the UV monitoring system. The static on–off $I–t$ characteristics of the system measured at b) different amount of lights (L1-L4) with different position of the index finger (I1-I3) and c) different position of the thumb (T1-T3), index finger (I1-I3), middle finger (M1-M3), ring finger (R1-R3), and little finger (L1-L3), which are measured separately with 4 lights on. d) The dynamic on–off photoresponse behaviors of the UV monitoring system in a series of motion combination with 4 lights on. All the measurements are conducted in a dark box.

**ADVANCED
SCIENCE NEWS**
www.advancedsciencenews.com

**ADVANCED
FUNCTIONAL
MATERIALS**
www.afm-journal.de

shown in Figure 7c. It is clear that the photocurrents are highly responsive to the finger positions, providing high possibility for realizing an effective detection of the movement of the mechanical arms. Moreover, the dynamic time dependent on/off photoresponse of the system in different motion states (see details in Figure S9, Supporting Information) is measured at a bias of 3 V, as shown in Figure 7d. The photocurrents present a stable and fast response when the PDs are set in the motion combination, which are mainly due to the angle-related effective area exposed to UV light compared with the static state. Besides, the deformability of the configurable PDs has also been measured after the same motion combination more than 100 times. Noteworthy, they can keep high photoresponse current and speed after a series of motion combination. Considering the facile and cost-effective feature of the electrospinning technique, the electrospun TiO_2 NFM with ultrahigh flexibility shows high potential for the application in flexible optoelectronics in the future.

3. Conclusions

In conclusion, we have demonstrated an effective method for the preparation of low-cost ultra-flexible TiO_2 NFMs via the combination of element doping and electrospinning technique. Compared with the pristine TiO_2 NFM-based PD, the 2 mol% Y^{3+}-doped TiO_2 NFM-based PD shows remarkably improved flexibility, where its original high-performance maintains when bending in different states (angles, radius, and spiral). More intriguingly, the PD can remain ≈60% photocurrent of the initial level when bending at ≈145° for about 20 000 cycles, enabling it suitable for the application in the high-performance wearable UV PDs. The doped Y^{3+} element is prone to distribute at the grain boundary of the TiO_2 polycrystalline, which could effectively inhibit the grain growth and reduce the surface defects and provides more slip systems when bending, and the microcrack could be sufficiently decreased and the breaking point of nanofiber is enhanced when bending different cycles. Finally, a real time wearable PD has been built for the detection of UV illumination by installing the PDs in a robot arm, where the exact detection of the UV density has been achieved in different motion states. This work would provide a promising avenue for the design and application of multifunctional inorganic material for real-time wearable UV sensors, as well as wearable electronic devices.

4. Experimental Section

Preparation of Flexible Y^{3+}-Doped TiO_2 Nanofibrous Membranes: The preparation of Y^{3+}-doped TiO_2 NFMs was performed by combining the electrospinning technique and the subsequent thermal annealing process, as follows: First, 2.94 mL tetrabutyl titanate and an appropriate amount of yttrium nitrate hexahydrate were completely dissolved in 1.75 mL absolute ethanol and 1.71 mL acetic acid with vigorous stirring in an ice-water bath for 30 min. Then, the solution was mixed with a 7 wt% polyvinylpyrrolidone (PVP) ethanol solution in ambient conditions by magnetic stirring for several hours to produce a transparent and homogeneous solution. Subsequently, the solution was transferred into a 5 mL syringe with a steel needle tip of 0.41 mm inner diameter. The positive bias connected to the needle tip and the negative bias

connected to the substrate was 10 and −2 kV, respectively. The distance between the needle tip and the substrate was 15 cm, and the feeding speed of the precursor was 0.02 mm min⁻¹. The relative humidity of the surroundings was kept below 35%. Finally, the as-spun hybrid fibrous membranes were exposed to a low temperature treatment at 90 °C for 2 h and then thermal treated in air for 2 h at 600 °C at a heating rate of 2 °C min⁻¹ to finally achieve the Y^{3+}-doped TiO_2 NFMs.

Fabrication of Devices: Symmetric (50 × 50 mm) contact electrodes (thickness of ≈70 nm) with a uniform channel length of 50 μm were deposited on the as-prepared Y^{3+}-doped TiO_2 NFMs through electron beam evaporation using a lithographic copper shadow mask.[44] For the construction of the real-time wearable UV irradiation monitor, copper wires were attached onto the Au/Cr electrodes by silver paste. The PDs were installed on the joints of a remote-controlled mechanical arm (Hangzhou Hailing Zhidian Technology co. LTD) which was placed into a home-made camera obscura (1000 × 1000 mm) installed with four UV irradiation lights (20W, UV-B range) in four corners. The other side of the copper wires was attached onto a glass sheet with silver paste, enabling the following photoelectric measurements.

Characterization: The microstructure and phase analysis of the pristine TiO_2 and the Y^{3+}-doped TiO_2 NFMs were studied by the XRD using a Bruker D8-A25 diffractometer. The morphological characterization of the NFMs was carried out by a FESEM (JSM-6701F), and further characterizations were based on the HRTEM (TECNAI G2 S-TWIN) with an EDS equipment. The component elements and their chemical environments of the as-prepared membranes were revealed by a XPS (PHI 5000C, Mg K_α radiation) with C 1s peak at 284.4 eV as standard signal. The optical properties were investigated by optical diffuse absorption spectra using a UV–vis spectrophotometer (Hitachi U-4100) with an integrating sphere attachment. Photoelectric properties, that is, I–V and I–t, were measured on a program-controlled semiconductor characterization system (Keithley 4200SCS, USA). A 75 W Xe lamp equipped with a monochromator was used as the light source and a NOVA II power meter (OPHIR photonics) was utilized to measure the light power density. The photoelectric performances of the PDs in different bending states (i.e., angles, radii and spiral) were measured by attaching the PDs on proper models. For the measurements of the fatigue strength, the planar PDs were attached on a PET as substrate and continuous cyclic bending for different time using a fiber tensile tester (XQ-1C, Shanghai Lipu Instrument Research Center Co., Ltd., China) and followed by an I–V measurement to estimate its photocurrent degradation. The photoelectric performances of the real-time wearable UV irradiation monitoring system were measured in various movement combinations. All the measurements were conducted under ambient conditions.

Supporting Information

Supporting Information is available from the Wiley Online Library or from the author.

Conflict of Interest

The authors declare no conflict of interest.

[1] a) P. E. Glaser, *Science* **1968**, *162*, 857; b) S. Y. Li, Y. Zhang, W. Yang, H. Liu, X. S. Fang, *Adv. Mater.* **2020**, *32*, 1905443.

[2] a) H. Chen, K. Liu, L. Hu, A. A. Al-Ghamdi, X. S. Fang, *Mater. Today* **2015**, *18*, 493; b) N. Nasiri, R. Bo, T. F. Hung, V. A. Roy, L. Fu, A. Tricoli, *Adv. Funct. Mater.* **2016**, *26*, 7359; c) F. Teng, W. Ouyang, Y. Li, L. Zheng, X. S. Fang, *Small* **2017**, *13*, 1700156; d) X. Xu, J. Chen, S. Cai, Z. Long, Y. Zhang, L. Su, S. He, C. Tang, P. Liu, H. Peng, X. S. Fang, *Adv. Mater.* **2018**, *30*, 1803165.

[3] a) H. Fang, C. Zheng, L. Wu, Y. Li, J. Cai, M. Hu, X. S. Fang, R. Ma, Q. Wang, H. Wang, *Adv. Funct. Mater.* **2019**, *29*, 1809013; b) Y. Chen, Y. Lu, M. Liao, Y. Tian, Q. Liu, C. Gao, X. Yang, C. Shan, *Adv. Funct. Mater.* **2019**, *29*, 1906040.

[4] a) Z. Zhu, Y. Gu, S. Wang, Y. Zou, H. Zeng, *Adv. Electron. Mater.* **2017**, *3*, 1700281; b) J. Yao, G. Yang, *Small* **2018**, *14*, 1704524.

[5] a) S. Cai, X. Xu, W. Yang, J. Chen, X. S. Fang, *Adv. Mater.* **2019**, *31*, 1808138; b) K. P. Bera, G. Haider, M. Usman, P. K. Roy, H.-I. Lin, Y.-M. Liao, C. R. P. Inbaraj, Y.-R. Liou, M. Kataria, K.-L. Lu, Y.-F. Chen, *Adv. Funct. Mater.* **2018**, *28*, 1804802.

[6] a) Z. Wang, H. Wang, B. Liu, W. Qiu, J. Zhang, S. Ran, H. Huang, J. Xu, H. Han, D. Chen, *ACS Nano* **2011**, *5*, 8412; b) K. Du, G. Liu, X. Chen, K. Wang, *J. Electrochem. Soc.* **2015**, *162*, E251.

[7] J. Song, X. Wang, J. Yan, J. Yu, G. Sun, B. Ding, *Sci. Rep.* **2017**, *7*, 1636.

[8] X. Obradors, T. Puig, M. Gibert, A. Queralto, J. Zabaleta, N. Mestres, *Chem. Soc. Rev.* **2014**, *43*, 2200.

[9] A. Blanco, C. López, R. Mayoral, H. Míguez, F. Meseguer, A. Mifsud, J. Herrero, *Appl. Phys. Lett.* **1998**, *73*, 1781.

[10] S. Chen, M. Yu, W.-P. Han, X. Yan, Y.-C. Liu, J.-C. Zhang, H.-D. Zhang, G.-F. Yu, Y.-Z. Long, *RSC Adv.* **2014**, *4*, 46152.

[11] J. Chen, Z. Li, F. Ni, W. Ouyang, X. S. Fang, *Mater. Horiz.* **2020**, *7*, 1828.

[12] Y. Wang, J. Cheng, M. Shahid, M. Zhang, W. Pan, *RSC Adv.* **2017**, *7*, 26220.

[13] P. Parreira, E. Torres, C. Nunes, C. N. de Carvalho, G. Lavareda, A. Amaral, M. J. Brites, *Sens. Actuators, B* **2012**, *161*, 901.

[14] K. Deng, L. Li, *Adv. Mater.* **2014**, *26*, 2619.

[15] Z. Lao, D. Pan, H. Yuan, J. Ni, S. Ji, W. Zhu, Y. Hu, J. Li, D. Wu, J. Chu, *ACS Nano* **2018**, *12*, 10142.

[16] a) J. Xue, T. Wu, Y. Dai, Y. Xia, *Chem. Rev.* **2019**, *119*, 5298; b) S. Zhang, H. Liu, N. Tang, J. Ge, J. Yu, B. Ding, *Nat. Commun.* **2019**, *10*, 1458.

[17] X. Yu, X. Wu, Y. Si, X. Wang, J. Yu, B. Ding, *Macromol. Rapid Commun.* **2019**, *40*, 1800931.

[18] H. Chong, G. Wei, H. Hou, H. Yang, M. Shang, F. Gao, W. Yang, G. Shen, *Nano Res.* **2015**, *8*, 2822.

[19] M. Xi, X. Wang, Y. Zhao, Q. Feng, F. Zheng, Z. Zhu, H. Fong, *Mater. Lett.* **2014**, *120*, 219.

[20] A. J. Molina-Mendoza, A. Moya, R. Frisenda, S. A. Svatek, P. Gant, S. Gonzalez-Abad, E. Antolin, N. Agraït, G. Rubio-Bollinger, D. P. de Lara, *J. Mater. Chem. C* **2016**, *4*, 10707.

[21] R. Zhang, X. Wang, J. Song, Y. Si, X. Zhuang, J. Yu, B. Ding, *J. Mater. Chem. A* **2015**, *3*, 22136.

[22] W. Han, F. Cui, Y. Si, X. Mao, B. Ding, H. Kim, *Small* **2018**, *14*, 1801963.

[23] A. Banerjee, D. Bernoulli, H. Zhang, M.-F. Yuen, J. Liu, J. Dong, F. Ding, J. Lu, W. Dao, W. Zhang, *Science* **2018**, *360*, 300.

[24] H. Shan, X. Wang, F. Shi, J. Yan, J. Yu, B. Ding, *ACS Appl. Mater. Interfaces* **2017**, *9*, 18966.

[25] W. Tian, T. Zhai, C. Zhang, S. L. Li, X. Wang, F. Liu, D. Liu, X. Cai, K. Tsukagoshi, D. Golberg, *Adv. Mater.* **2013**, *25*, 4625.

[26] a) L. Huang, J. Yang, X. Wang, J. Han, H. Han, C. Li, *Phys. Chem. Chem. Phys.* **2013**, *15*, 553; b) S. Gaarenstroom, N. Winograd, *J. Chem. Phys.* **1977**, *67*, 3500.

[27] F. Cao, L. Meng, M. Wang, W. Tian, L. Li, *Adv. Mater.* **2019**, *31*, 1806725.

[28] W. Yang, K. Hu, T. Feng, J. Weng, Y. Zhang, X. S. Fang, *Nano Lett.* **2018**, *18*, 4697.

[29] a) F. P. G. de Arquer, A. Armin, P. Meredith, E. H. Sargent, *Nat. Rev. Mater.* **2017**, *2*, 16100; b) W. Ouyang, F. Teng, X. S. Fang, *Adv. Funct. Mater.* **2018**, *28*, 1707178.

[30] a) Z. Lou, G. Shen, *Adv. Sci.* **2016**, *3*, 1500287; b) C. Xie, F. Yan, *Small* **2017**, *13*, 1701822.

[31] a) S. Xu, Z. Yan, K.-I. Jang, W. Huang, H. Fu, J. Kim, Z. Wei, M. Flavin, J. McCracken, R. Wang, A. Badea, Y. Liu, D. Xiao, G. Zhou, J. Lee, H. U. Chung, H. Cheng, W. Ren, A. Banks, X. Li, U. Paik, R. G. Nuzzo, Y. Huang, Y. Zhang, J. A. Rogers, *Science* **2015**, *347*, 154; b) X. Xu, Y. Zuo, S. Cai, X. Tao, Z. Zhang, X. Zhou, S. He, X. S. Fang, H. Peng, *J. Mater. Chem. C* **2018**, *6*, 4866.

[32] C. Sa, X. Xu, X. Wu, J. Chen, C. Zuo, X. S. Fang, *J. Mater. Chem. C* **2019**, *7*, 13097.

[33] W. Kallel, S. Chaabene, S. Bouattour, *Physicochem. Probl. Miner. Process.* **2019**, *55*, 745.

[34] a) W. Zhang, K. Wang, S. Zhu, Y. Li, F. Wang, H. He, *Chem. Eng. J.* **2009**, *155*, 83; b) Q. Zhang, Y. Fu, Y. Wu, Y.-N. Zhang, T. Zuo, *ACS Sustainable Chem. Eng.* **2016**, *4*, 1794.

[35] J. H. Pan, W. I. Lee, *Chem. Mater.* **2006**, *18*, 847.

[36] X. Cheng, Z. Qi, G. Zhang, H. Zhou, W. Zhang, M. Yin, *Phys. B* **2009**, *404*, 146.

[37] T. Mongstad, A. Thøgersen, A. Subrahmanyam, S. Karazhanov, *Sol. Energy Mater. Sol. Cells* **2014**, *128*, 270.

[38] S. Huang, H. Wu, M. Zhou, C. Zhao, Z. Yu, Z. Ruan, W. Pan, *NPG Asia Mater.* **2014**, *6*, e86.

[39] a) M. A. Meyers, A. Mishra, D. J. Benson, *Prog. Mater. Sci.* **2006**, *51*, 427; b) Z. Li, M. Coll, B. Mundet, N. Chamorro, F. Vallès, A. Palau, J. Gazquez, S. Ricart, T. Puig, X. Obradors, *Sci. Rep.* **2019**, *9*, 5828.

[40] P. Zhang, Y. Yu, E. Wang, J. Wang, J. Yao, Y. Cao, *ACS Appl. Mater. Interfaces* **2014**, *6*, 4622.

[41] M. H. Oh, M. G. Cho, D. Y. Chung, I. Park, Y. P. Kwon, C. Ophus, D. Kim, M. G. Kim, B. Jeong, X. W. Gu, J. Jo, J. M. Yoo, J. Hong, S. McMains, K. Kang, Y.-E. Sung, A. P. Alivisatos, T. Hyeon, *Nature* **2020**, *577*, 359.

[42] L. Wu, Y. Zhang, Y.-G. Jung, J. Zhang, *J. Power Sources* **2015**, *299*, 57.

[43] H. Shan, Y. Si, J. Yu, B. Ding, *Chem. Eng. J.* **2020**, *382*, 122909.

[44] L. Su, Y. Zhu, X. Xu, H. Chen, Z. Tang, X. S. Fang, *J. Mater. Chem. C* **2018**, *6*, 7776.

[45] Z. Lou, X. Yang, H. Chen, Z. Liang, *J. Semicond.* **2018**, *39*, 024002.

[46] Z. Zheng, F. Zhuge, Y. Wang, J. Zhang, L. Gan, X. Zhou, H. Li, T. Zhai, *Adv. Funct. Mater.* **2017**, *27*, 1703115.

[47] M. Y. Lee, J. Hong, E. K. Lee, H. Yu, H. Kim, J. U. Lee, W. Lee, J. H. Oh, *Adv. Funct. Mater.* **2016**, *26*, 1445.

[48] Z. Zheng, L. Gan, J. Zhang, F. Zhuge, T. Zhai, *Adv. Sci.* **2017**, *4*, 1600316.